scientific reports

OPEN

# Photocatalytic activity and anticancer properties of green synthesized ZnO-MgO-$Mn_2O_3$ nanocomposite via *Ocimum basilicum* L. seed extract

**Razieh Hazrati Saadabadi[1], Fatemeh Shariatmadar Tehrani[1]✉, Zahra Sabouri[2,3] & Majid Darroudi[4]✉**

**Green synthesis using plant extracts such as *Ocimum basilicum* L. (OBL) seed has attracted attention due to its sustainable and environmentally friendly nature. In this study, ZnO-MgO-$Mn_2O_3$ nanocomposites were synthesized using OBL seed extract at two different calcination temperatures of 500 °C and 600 °C, and evaluated in terms of photocatalytic application and cytotoxicity. Phytochemicals in OBL seeds act as reducing and masking agents in the production route, which leads to the formation of nanomaterials with unique properties. Characterization techniques, including XRD, FE-SEM, and DRS were used to analyze the structural, morphological, and optical features of the nanocomposite. XRD results confirmed increasing crystal size from ~ 32 nm (500 °C) to ~ 84 nm (600 °C). Also, FE-SEM images showed formation of irregularly shaped nanocomposites and the EDX spectra of the samples confirmed the presence of zinc, magnesium, manganese, and oxygen elements. The photocatalytic behavior of the nanocomposite cacined at 500 °C was investigated for different organic pollutants. Removal percentages of 97% for Eriochrome Black T dye (pH = 10 for 90 min), 99% for methylene blue dye (pH = 10 for 60 min), 89% for methyl orange dye (pH = 10 for 105 min), and 86.9% for Rhodamine B dye (pH = 3 for 90 min) were obtained. Moreover, the cytotoxicity of the synthesized nanocomposite at 500 °C was evaluated on the 4T1 cell line to investgate its effect on biological systems, and the $IC_{50}$ value was obtained around 323 µg/mL.**

**Keywords** Plant-mediated synthesis, ZnO-MgO-$Mn_2O_3$ nanocomposite, *Ocimum basilicum* L. seed, Anticancer, Photocatalytic

**Abbreviations**

| | |
|---|---|
| ZnO | Zinc oxide |
| MgO | Magnesium oxide |
| $Mn_2O_3$ | Manganese (III) oxide |
| ROS | Reactive oxygen species |
| DRS | Diffuse reflectance spectroscopy |
| OBL | *Ocimum basilicum* L. |
| MTT | 3-(4,5-dimethylthiazol-2-yl)-2,5-diphenyltetrazolium bromide |
| MB | Methylene blue |
| RhB | Rhodamine B |
| MO | Methyl orange |
| DI | Deionized |
| EBT | Eriochrome black T |

[1]Faculty of Physics, Semnan University, Semnan 35195-363, Iran. [2]Department of Medical Biotechnology and Nanotechnology, Faculty of Medicine, Mashhad University of Medical Sciences, Mashhad, Iran. [3]Student Research Committee, Mashhad University of Medical Sciences, Mashhad, Iran. [4]Nuclear Medicine Research Center, Mashhad University of Medical Sciences, Mashhad, Iran. ✉email: f_tehrani@semnan.ac.ir; majiddarroudi@gmail.com; darroudim@mums.ac.ir

| | |
|---|---|
| DMSO | Dimethyl sulfoxide |
| DMEM | Dulbecco's modified eagle medium |
| $IC_{50}$ | Half-maximal inhibitory concentration |
| FT-IR | Fourier transform-Infrared |
| UV-Vis | Ultraviolet-visible |
| XRD | X-ray diffraction |
| EDX | Energy dispersive X-ray |
| FE-SEM | Field emission scanning electron microscopy |
| PSA | Particle size analyzer |

In recent years, nanotechnology has emerged as a transformative field with wide applications in energy, medicine, and environmental sustainability. Metal oxide nanocomposites are innovative materials that combine several metal oxide components at the nanoscale, offering improved properties and diverse applications[1,2]. Trimetal oxide nanocomposites are powerful tools for environmental remediation, which consist of three different metal oxides. They have emerged as promising materials for environmental remediation due to their unique properties and synergistic effects. Some of the key properties of these materials are: 1: High surface area: This property increases the capacity to absorb pollutants and turns them into efficient absorbers, 2: Strong oxidation and reduction properties: trimetallic oxides often show strong oxidation and reduction properties, enabling them to degrade pollutants through oxidation-reduction reactions, 3: Photocatalytic activity: when these materials are exposed to light, they can produce reactive oxygen species (ROS) that can decompose organic pollutants[1,3–5]. The synergistic effects of the constituent metal oxides give rise to the properties of new materials with a wide range of potential applications. These nanocomposites take advantage of the synergistic effects of their components, leading to improved performance compared to their counterparts. Synthesis of nanocomposites can be achieved through traditional chemical methods as well as innovative green synthesis techniques, each offering unique advantages and considerations. The chemical method involves the controlled manipulation of chemical reactions to synthesize metal oxide nanocomposites. Researchers can adjust the composition, size, shape, and structure of nanocomposites by carefully selecting metal precursors, solvents, and reaction conditions[6]. Traditional methods of large-scale synthesis of nanomaterials, such as chemical and physical methods, have disadvantages including high costs, negative environmental effects, and energy consumption[7]. In response to these challenges, "green synthesis" has emerged as a promising alternative. This technique uses organic materials such as plant extracts as reducing and stabilizing agents in the process of producing nanoparticles[8,9]. Incorporating organic materials such as plant extracts into the synthesis process not only reduces the environmental impact but also opens up exciting avenues for applications in various fields, from environmental remediation to biomedicine[10]. The green synthesis method focuses on sustainable and eco-friendly procedures for producing metal oxide nanocomposites[11–13]. By using natural sources such as plant extracts, microbes, or bio-waste as reducing and stabilizing agents, researchers can minimize the use of toxic chemicals and reduce the environmental impact of the synthesis process[14–17]. The synthesis process begins with the extraction of plant components, especially polyphenols, which act as reducing and stabilizing agents[18,19]. These bioactive compounds play a key role in the formation and stability of nanocomposite by coordinating with metal ions during the synthesis process.

Pollutants such as heavy metals, organic dyes and pharmaceutical compounds can have significant adverse effects on human health. Exposure to these pollutants can lead to a variety of health problems including: cancer, neurological disorders, respiratory problems, and skin problems. Zinc oxide (ZnO) nanoparticles (a key component of nanocomposites) exhibit unique properties such as high surface area, excellent photocatalytic activity, and biocompatibility[20]. The use of ZnO nanoparticles in photocatalysis and their potential cytotoxicity towards cancer cells show the diverse range of applications that nanomaterials can have in environmental improvement and health care. The challenges faced by ZnO nanoparticles, such as the fast recombination of electron–hole pairs and poor absorption of visible light, highlight the importance of exploring nanocomposites and modifications to enhance their performance[21]. Magnesium oxide (MgO) nanoparticles (another essential component) have properties that increase the overall performance of the nanocomposite. MgO nanoparticles have been widely studied for their photocatalytic activity, biocompatibility, and potential applications in drug delivery and imaging methods[22,23]. In addition, MgO nanoparticles have a band gap in the UV region, which enables them to efficiently absorb UV light and generate electron–hole pairs that facilitate redox reactions for advanced photocatalysis. Their ability to generate reactive oxygen species (ROS) makes them promising cytotoxic agents against cancer cells[22]. Manganese oxide nanoparticles ($Mn_2O_3$) bring more advantages to the nanocomposite because of their high surface area, visible light absorption, and catalytic attributes[24]. $Mn_2O_3$ nanoparticles have been shown in applications such as water purification, supercapacitors, and targeted cancer treatment[25]. Their cytotoxic effects on cancer cells, primarily cause oxidative stress and damage to cellular components[26]. By exploring the synergistic effects of ZnO, MgO, and $Mn_2O_3$ in a nanocomposite form through green synthesis, researchers aim to unlock new possibilities for efficient photocatalysis and targeted cytotoxicity toward cancer cells, shedding light on the promising applications of nanotechnology in addressing key challenges in environmental and biomedical domains.

In recent years, many studies have been conducted on the synthesis of metal oxide nanocomposites and their photocatalytic properties and cytotoxicity. In 2020, Zgura et al. synthesized ZnO-CdS nanocomposite by a simple chemical precipitation method and investigated its photocatalytic effect for removing methylene blue dye and its toxicity effect on BJ cells[27]. In 2021, Shubha et al. synthesized ternary ZnO/$Eu_2O_3$/NiO nanoparticles by a simple one-pot combustion method and its photocatalytic activity was investigated for the photodegradation of methylene blue[28]. In 2023, Yadav et al. synthesized $Cu_2O$/RGO nanocomposite using orange pulp extract as a reducing and stabilizing agent and used it as a catalyst for the photocatalytic degradation of DC in water samples[29]. In 2024, M. Abdelbar et al. synthesized CdSQDs@ZnCr-LDO/ZnO ternary nanocomposite by green sonochemical method and studied its photocatalytic effect in the degradation of Rhodamine B dye[30].

The objective of current research is a green synthesis of the new ternary ZnO-MgO-$Mn_2O_3$ nanocomposite through an environmentally friendly process using *Ocimum basilicum* L (OBL) plant extract. OBL extract is used in the synthesis of nanomaterials due to its rich composition of bioactive compounds, especially flavonoids that can act as reducing agents and facilitate the reduction of metal ions to form nanoparticles. They can also act as capping agents, stabilizing nanoparticles and preventing their aggregation. On the other hand, flavonoids are generally biocompatible, which is important for the development of nanomaterials for biomedical applications. The photocatalytic ability of the synthesized nanocomposite to remove different dyes (MB, EBT, MO, and RhB) from aqueous solution under UV light irradiation was investigated. In addition, a cytotoxicity evaluation of the synthesized nanocomposite performed to study its effectiveness against cancer cells. This study undeniably verify that the ZnO-MgO-$Mn_2O_3$ nanocomposite has promising applications in a wide range of applications in the fields of biomedicine and environmental protection.

## Experiential section

### Materials

The chemicals were used without undergoing any purification. $Zn(NO_3)_2$. $6H_2O$, $Mg(NO_3)_2$. $6H_2O$, $Mn(NO_3)_2$. $4H_2O$, methylene blue ($C_{16}H_{18}ClN_3S$), rhodamine B ($C_{28}H_{31}ClN_2O_3$), eriochrome black T ($C_{20}H_{12}N_3O_7SNa$), methyl orange ($C_{14}H_{14}N_3NaO_3S$), HCl, and NaOH were bought from Sigma Co. In this project, deionized (DI) water was used to make all solutions.

### Preparation of nanocomposite

To prepare the OBL plant extract for the synthesis of the nanocomposite, OBL plant were first collected from areas of Hezar Masjed in Dargaz, Iran, and the seeds were separated from its flowers. After that, they were washed twice with distilled water and dried in the dark. Next, 1 g of dried plant seeds was mixed with deionized water (0.1 L) and stirred for 120 min (60 °C). Then it was filtered using the Whatman 42 paper for twice and stored in a cool place to be used in the synthesis process. To synthesize ZnO-MgO-$Mn_2O_3$ nanocomposite, the solutions of zinc nitrate (50 mL), magnesium nitrate (50 mL), and manganese nitrate (50 mL) with a concentration of 0.5 M were prepared separately. Later these solutions were mixed and stirred on a magnetic stirrer (700 rpm) for 45 min. Meanwhile, 30 mL of OBL seed extract was added to the previous step solution and kept at 80 °C for 6 h to form a gel. Finally, the obtained gel was dried for 8 h at 80 °C and then calcined at 500 °C and 600 °C for 2 h to form ZnO-MgO-$Mn_2O_3$ nanocomposites[31]. Figure 1 schematically shows the stages of nanocomposite synthesis.

### Characterization

The XRD patterns of the green-synthesized ZnO-MgO-$Mn_2O_3$ nanocomposites calcined at 500 °C and 600 °C were recorded utilizing an X-ray diffractometer at $2\theta = 10–80^{\circ}$. FT-IR analysis was used to identify functional groups in nanomaterials (in the range 400–4000 $cm^{-1}$). UV-Vis-DRS analysis has been used to study the optical properties and band gap energy of the nanocomposites. FE-SEM analysis is used to investigate the morphology of nanocomposite which provides high-resolution images. Digimizer software measured the particle size distribution according to FE-SEM images. EDX analysis has been employed to determine atomic and weight percentages of elements in the nanocomposite, which gives insight into the composition and distribution of elements in the sample. These characterization techniques provide detailed information on the structural, morphological, and optical attributes of the ZnO-MgO-$Mn_2O_3$ nanocomposite, contributing to a comprehensive understanding of its properties and potential applications.

### Trials about photodegradation

The efficiency of ZnO-MgO-$Mn_2O_3$ nanocomposite was investigated for removal of MB, MO, EBT, and RhB dyes from aqueous solution under UVA light irradiation. Initially, 27.9 mg of the photocatalyst was introduced into 100 mL of each of the dye solutions ($10^{-5}$ M). Before exposure to UV light, the combined solutions underwent agitation in darkness for 45 min, which allowed for the equilibrium of dye molecules' adsorption and desorption. The photodegradation process commenced with the activation of UVA light, which catalyzed the degradation of the dyes. At regular intervals of 15 min, an amount of the solution (2 mL) was removed to monitor the progress of the degradation route. This periodic sampling ensured continuous assessment of degradation efficiency over time. Next, the collected samples were centrifuged to separate the catalyst from the solution (12,000 rpm for 10 min). Then, the absorption of the samples was measured using UV-Vis spectroscopy. The degradation efficiency of dyes was determined using a specified formula (Eq. 1), which includes the initial concentration of dyes and the remaining concentrations after the photodegradation process[32,33].

$$\text{Degradation }(\%) = [(A_0 - A_t)/A_0] \times 100 \tag{1}$$

where $A_t$ indicates absorbance after a specific period and $A_0$ indicates starting absorbance. Reaction kinetic models are valuable tools for explaining the time-dependent correlation between the system's operational parameters and the degradation rate of organic pollutants or the inactivation rate of microorganisms. The following relationships can be applied to find pseudo-first-order kinetic (Eq. 2)[34,35] and pseudo-second-order kinetic behaviors (Eq. 3)[36,37].

$$Ln\left(\frac{C_t}{C_0}\right) = K_{obs}t \tag{2}$$

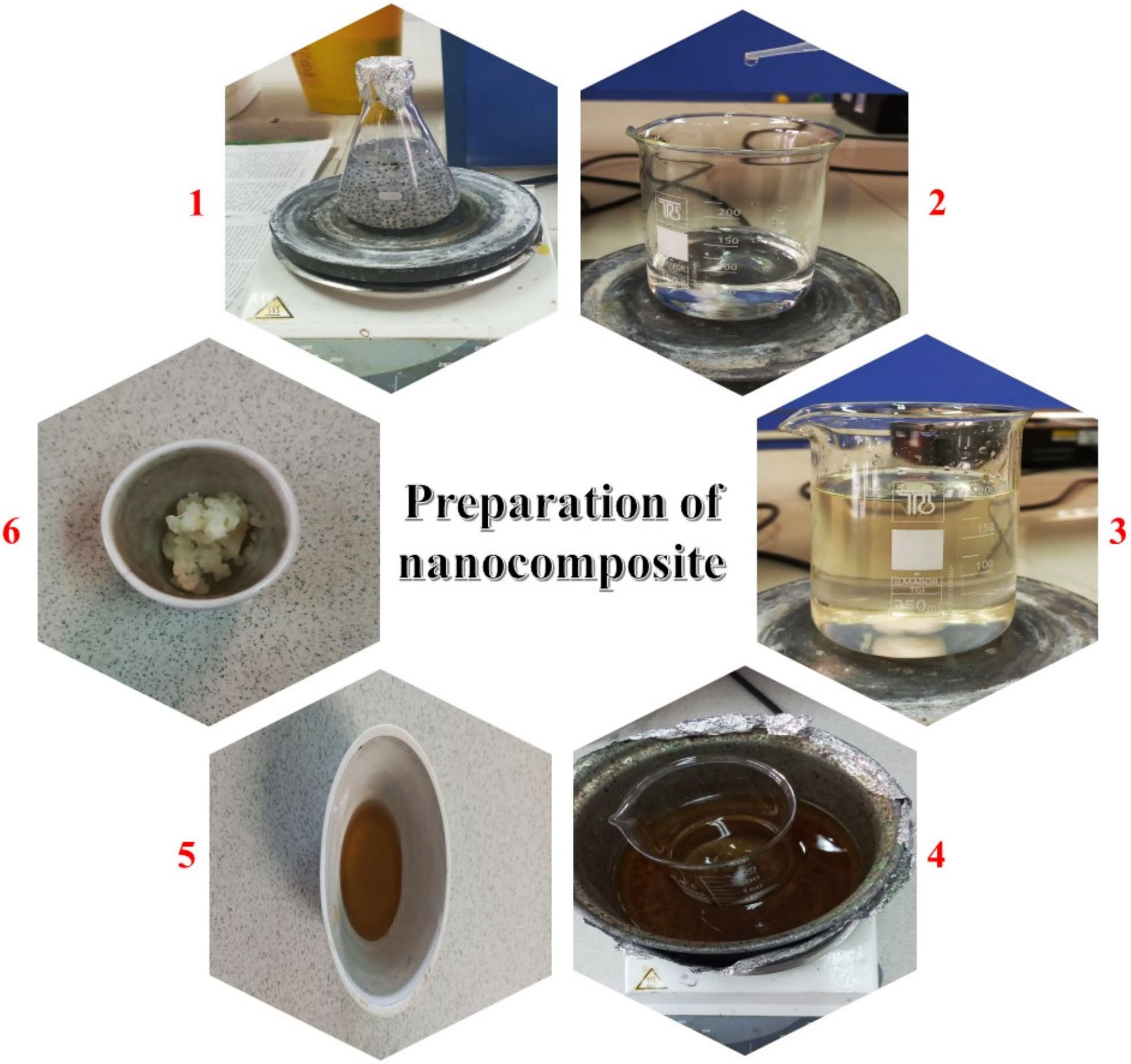

**Fig. 1**. Schematic steps of ZnO-MgO-$Mn_2O_3$ nanocomposite synthesis, **(1)** Preparation of extract, **(2)** Preparation of salt solutions, **(3)** Mix the salt solutions with the extract, **(4)** The formation of gel, **(5)** Dried at 80 °C for 8 h, **(6)** Calcination at 500 °C and 600 °C for 2 h.

$C_0$: Initial concentration, $C_t$: Concentration at a certain time, and $K_{obs}$ is the reaction rate constant.

$$\frac{t}{q_t} = \frac{1}{Kq_e^2} + \frac{t}{q_e} \tag{3}$$

where $q_e$ is the adsorbent quantity at equilibrium, and $q_t$ is the amount absorbed at time t.

## Results and discussion

### XRD

Figure 2 shows the XRD patterns of the ternary metal oxide nanocomposite (ZnO-MgO-$Mn_2O_3$). The diffraction peaks were identified and indexed based on the standard JCPDS database. The observed peaks at 2θ of 31.77, 34.43, 36.26, 47.55, 56.61, 62.87, 67.97, and 69.11° correspond to the (100), (002), (101), (102), (110), (103), (112), and (201) crystal planes of ZnO (JCPDS card # 01-079-0206)[38,39]. Similarly, the peaks at 2θ values of 36.93, 42.91, 62.3, and 74.69° can be assigned to the (111), (200), (220), and (311) crystal planes of MgO (JCPDS No#00-045-0946)[40,41]. Additionally, the peaks at 2θ values of 23.13, 32.95, 34.68, 38.23, 45.18, 55.19, and 65.8° are attributed to the (211), (222), (321), (400), (332), (440), and (622) crystal planes of $Mn_2O_3$ (JCPDS No # 00-041-1442)[42,43]. Scherrer's Eq. (4) was used to estimate the grain size of the nanomaterials, and the results

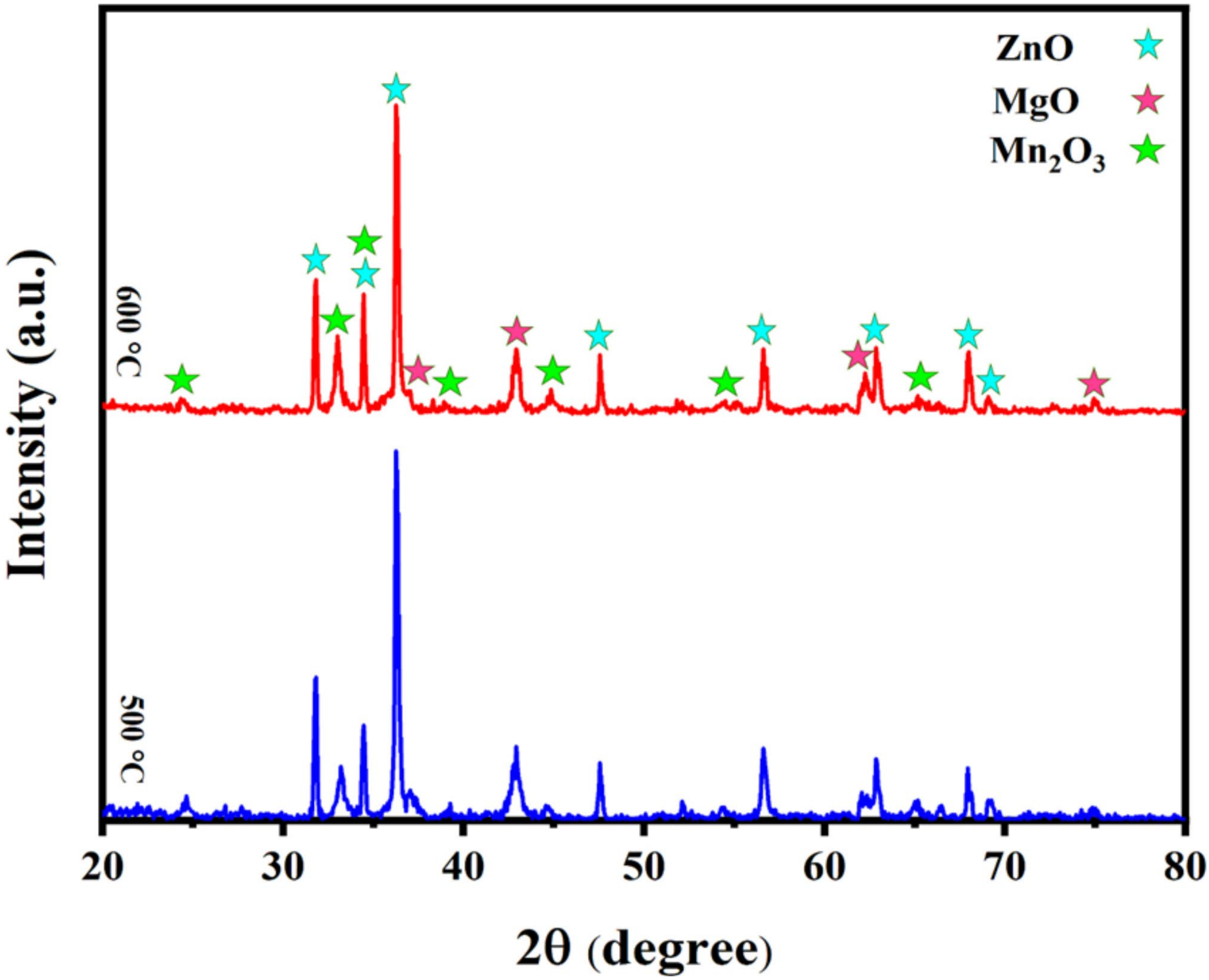

**Fig. 2**. XRD patterns of the synthesized ternary ZnO-MgO-$Mn_2O_3$ nanocomposites.

| Tem (°C) | Crystallinity (%) | *SSA ($m^2$/g) | *$\delta$ (line/$m^2$) | Grain size (nm) | *$\varepsilon$ |
|---|---|---|---|---|---|
| 500 | 51.64 | 39.27 | 1.8 | 32.2 | 2.86 |
| 600 | 54.29 | 32.42 | 1.3 | 38.9 | 4.10 |

**Table 1**. The crystallographic data and sample characteristics. *SSA: Specific surface area. *$\delta$: Dislocation-density. *$\varepsilon$: Micro strain.

show the increase in crystallite size with increasing calcination temperature[44,45]. Also, according to Eq. (5), the crystallinity (%) of the synthesized nanocomposites is estimated by comparing the area under the XRD peaks to the total area of the XRD pattern[46]. Furthermore, the dislocation density for the nanocomposites were derived using Eq. (6)[47], while Eq. (7) evaluated deformation or crystal defects in the nanocomposites in terms of strain[48,49]. On the other hand, Eq. (8) was used to compute the specific surface area (SSA)[50,51]. All calculated parameters are presented in Table 1.

$$D = 0.89\lambda \ / (\beta \ \ cos\theta\ ) \tag{4}$$

where $D$ is average crystallite size, $\lambda$ is X-ray wavelength, $\beta$ is full width at half maximum (FWHM) of the peak, and $\theta$ is the diffraction angle.

$$Crystallinity\ \ (\%) \ = \ \left({}^{A_{cp}}\!/_{A_T}\right) \ \times 100 \tag{5}$$

where $A_{cp.}$ is the region below crystalline peaks and $A_T$ is total area.

$$\delta = {}^{1}\!/_{D^2} \tag{6}$$

$\delta$ is dislocation density,

$$\varepsilon = {}^{\beta}\!/_{4\ tan\ \theta} \tag{7}$$

where $\varepsilon$ is the lattice strain, and

$$Specific\ \ surface\ \ area = {}^{6000}\!/_{\rho \times D} \tag{8}$$

$\rho$ is the density as determined from XRD analysis.

## FT-IR

FT-IR spectra of the synthesized nanocomposites are illustrated in Fig. 3. The prominent peak at 470 $cm^{-1}$ is an indicative of the metal-oxygen bond's stretching vibrations, suggesting excellent dispersion of the metal oxide nanocomposite[52]. Additionally, a distinct peak detected about 1460 $cm^{-1}$ corresponds to the stretching vibrations of the C–C bond, possibly originating from organic molecules in the OBL extract[53]. The absorption band at 3440 $cm^{-1}$ implies the presence of O–H group stretching vibrations[54]. The comparison of the FTIR spectrum of the OBL extract with the samples 500 °C and 600 °C shows that the intensity of the O–H peak is significantly lower for the nonocomposites. This shows that water molecules and hydroxyl groups are removed from the samples at high temperatures. Also, various characteristic absorption peaks present in the spectrum of OBL extract are absent in the spectra of the nanocomposites that verifies the removal of organic matter during the calcination process and the formation of a more crystalline metal oxide structure.

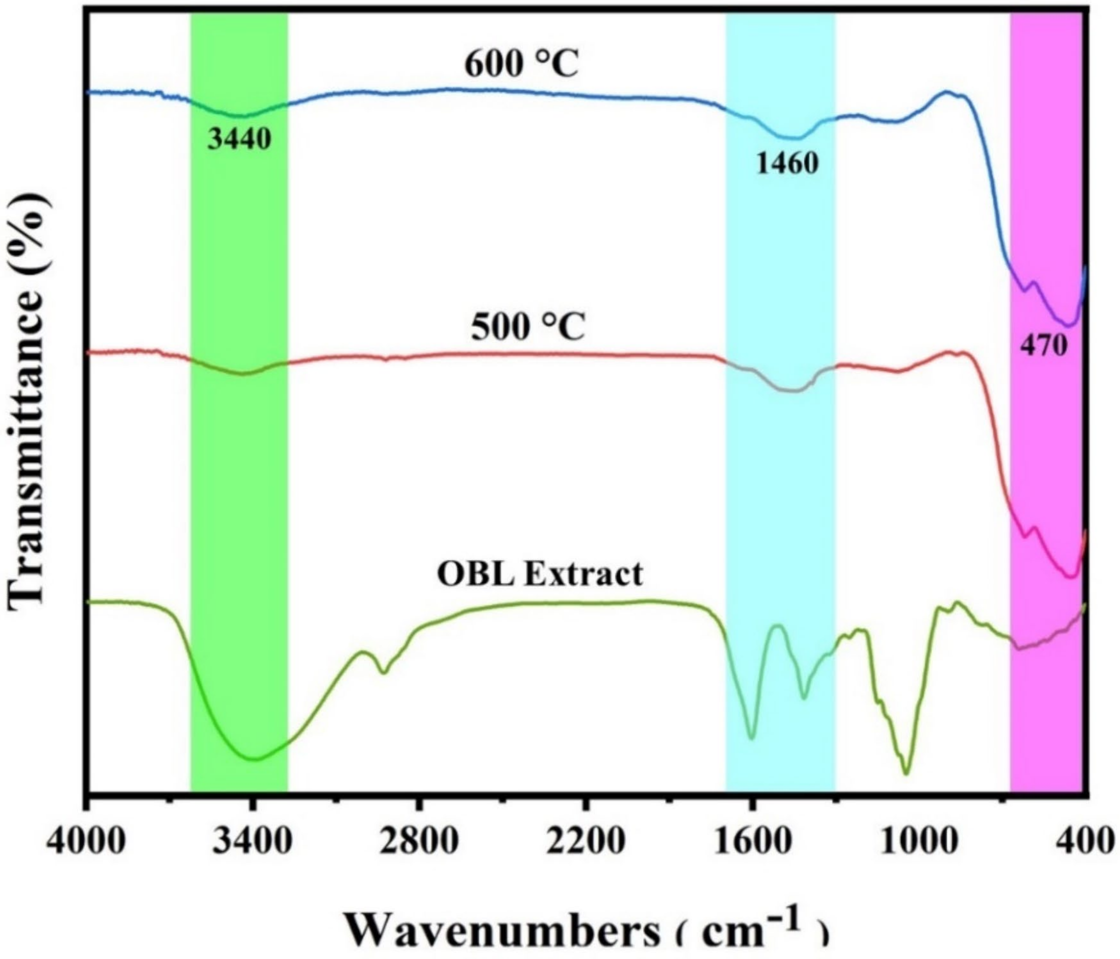

**Fig. 3**. FT-IR spectra of the synthesized ZnO-MgO-$Mn_2O_3$ ternary nanocomposites. The FTIR spectrum of OBL extract is included for comparison.

## Morphology study

FE-SEM images of ZnO-MgO-$Mn_2O_3$ nanocomposites calcined at 500 °C and 600 °C are shown in Figs. 4a and 5a, respectively. FE-SEM images indicate formation of relatively irregular particles for both nanocomposites, however, the nanocomposite calcined at 500 °C exhibits a more uniform appearance and smaller particle size than the 600 °C sample. To accurately analyse the images and determine the average particle size, FE-SEM images were processed using Digimizer software and analyzed using SPSS software. The particle size distribution curves obtained from the analysis are shown in Figs. 4b and 5b for the samples 500 °C and 600 °C, respectively. It should be noted that the results indicate a significant increase in the average particle size from 31.8 nm at 500 °C to 83.8 nm at 600 °C. To identify and quantify the constituent elements in the ZnO-MgO-$Mn_2O_3$ nanocomposites, EDX analysis was performed on the samples and Figs. 4c and 5c confirmes the presence of zinc, magnesium, manganese and oxygen in the synthesized samples. Also, the atomic and weight% of the elements are shown in a table in Figs. 4 and 5. Furthermore, the mapping images (Figs. 4d and 5d) show the elemental distribution in the synthesized nanocomposites, which confirms a uniform dispersion of the constituent elements throughout the samples.

## UV-Vis-DRS analysis

It is very important to understand the efficiency of a photocatalyst in photodegradation with key parameters such as band gap energy and absorption coefficient playing an important role[55]. The absorption spectra of the synthesized ZnO-MgO-$Mn_2O_3$ nanocomposites and their corresponding Tauc plot for band gap determinaion are revealed in Fig. 6a,b. It is noteworthy that both nanocomposites exhibit high absorption in a wide range of DRS absorption spectrum including visible and near-infrared regions as can be seen in Fig. 6a. This behaviour is promising in optical applications need high absorption of light such as photocatalytic reactions.

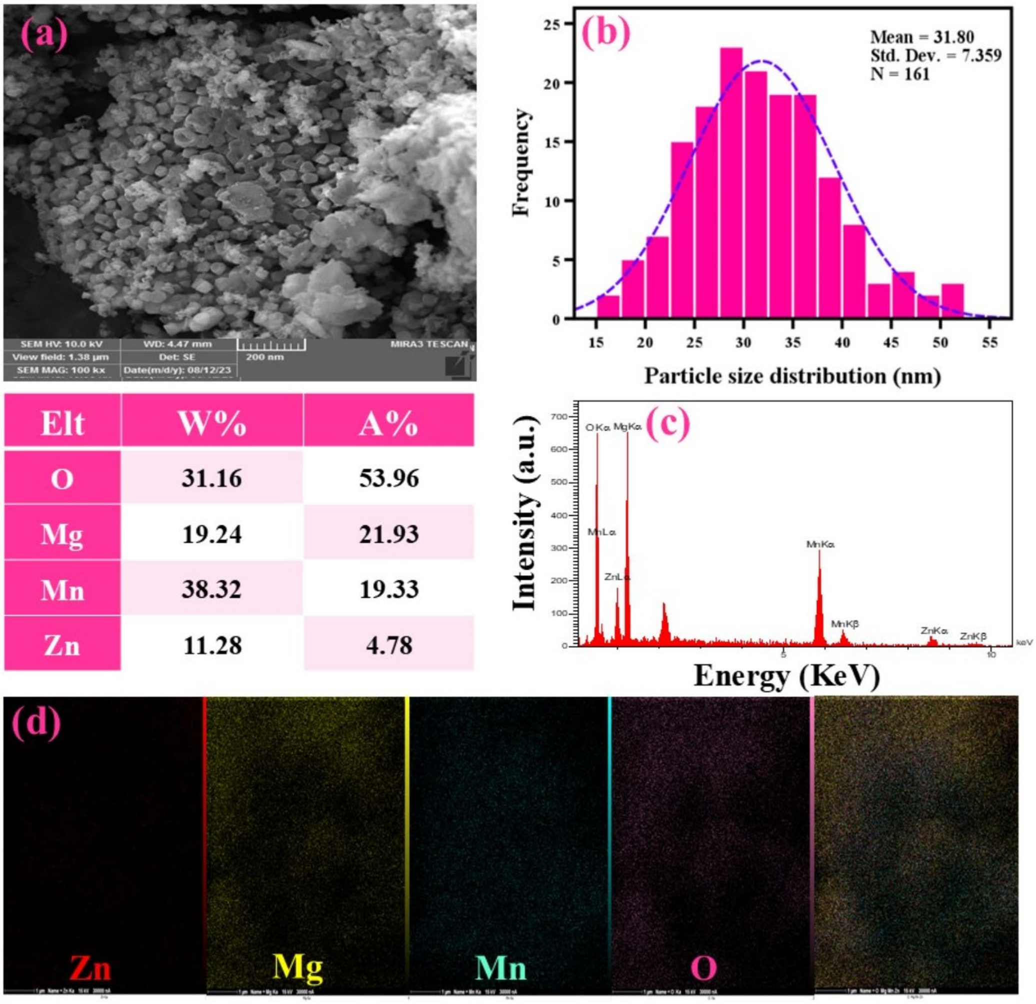

| Elt | W% | A% |
|---|---|---|
| O | 31.16 | 53.96 |
| Mg | 19.24 | 21.93 |
| Mn | 38.32 | 19.33 |
| Zn | 11.28 | 4.78 |

**Fig. 4**. (**a**) FE-SEM images of ZnO-MgO-$Mn_2O_3$ nanocomposite calcined at 500 °C, (**b**) particle size histograms; (**c**) EDX spectrum, and (**d**) mapping (**e**).

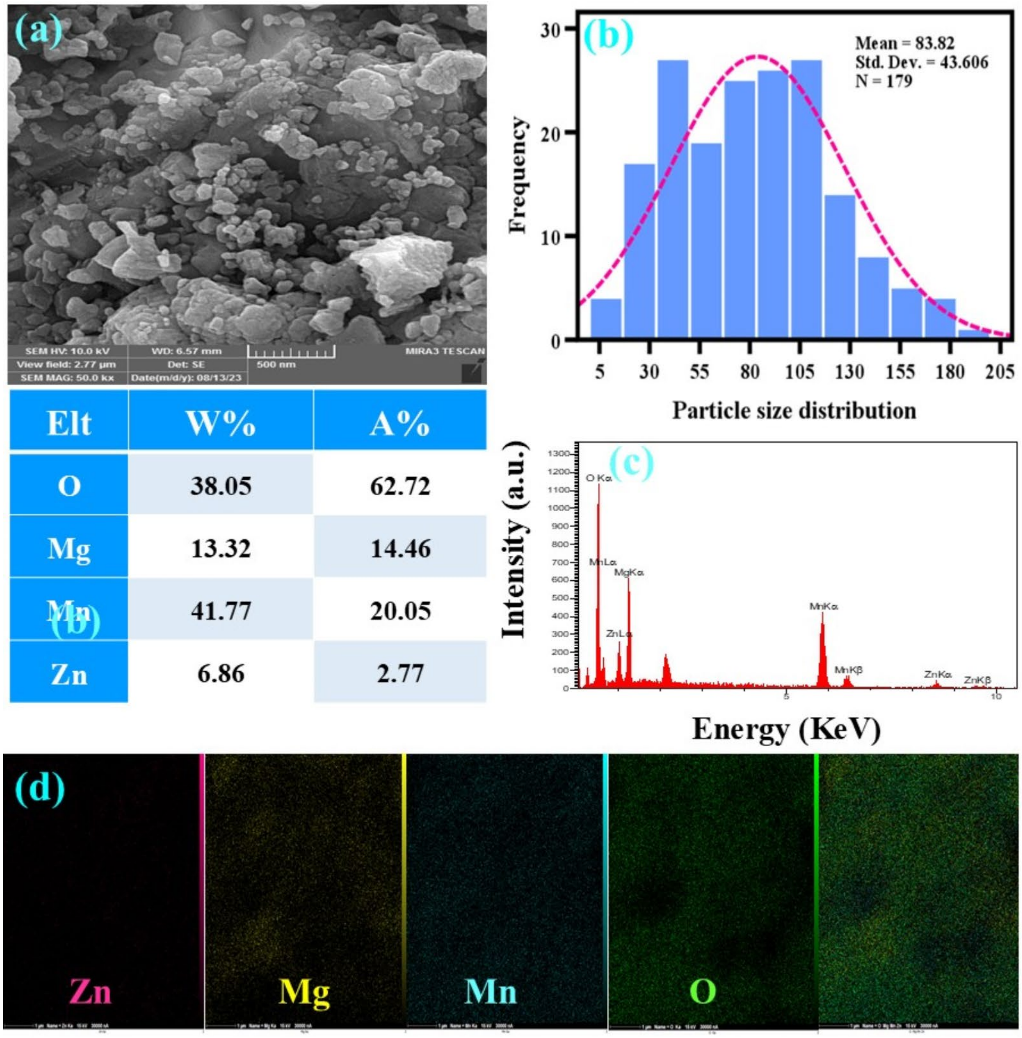

| Elt | W% | A% |
|---|---|---|
| O | 38.05 | 62.72 |
| Mg | 13.32 | 14.46 |
| Mn | 41.77 | 20.05 |
| Zn | 6.86 | 2.77 |

**Fig. 5**. (**a**) FE-SEM images of ZnO-MgO-$Mn_2O_3$ nanocomposite calcined at 600 °C, (**b**) particle size histograms; (**c**) EDX spectrum, and (**d**) mapping (**e**).

To determine the band gap of the nanocomposite, Eq. (9) (Tauc equation) was used and the band gap values are presented in Fig. 6b[56]. In addition, the Kubelka-Munk function Eq. (10) was used to accurately determine the absorption coefficient[57,58]. To obtain band gap values, it is necessary to use techniques such as linear fitting, which emphasizes its pivotal role in revealing the optical complexities of nanocomposites for potential applications in advanced photocatalysis

$$(\alpha\, h\nu\,)^{\frac{1}{n}}\;=A\,(h\nu\;-E_g) \tag{9}$$

where $\alpha$ is the absorption coefficient, $hv$ is photon energy, $A$ is a constant, $E_g$ is band gap energy, and $n$ is Tauc exponent (typically is 1/2 to 2 depending on the nature of the optical transition).

$$\alpha\;=F\,(R_\infty\,)=\frac{K}{S}=\frac{(1-R_\infty\,)^2}{2R_\infty} \tag{10}$$

F(R) is the Kubelka-Munk function; (R) is the reflectance of the sample.

The calculated band gaps of the ZnO–MgO-$Mn_2O_3$ nanocomposites calcined at 500 °C and 600 °C are 5.36 eV and 5.40 eV, respectively, as depicted in Fig. 6b. The results indicates that the increase in calcination temperature from 500 to 600 °C did not have much effect on the band gap values of the synthesized nanocomposites. The typical band gaps of constituent metal oxides are 3.5 eV, 5.2 eV, and 1.5 eV for ZnO, MgO, and $Mn_2O_3$, respectively, as reported in the literatures[59,60]. On the other hand, the absorption spectra of the synthesized nanocomposites obviously exhibit three distinct absorption egdes occurred at ~800 nm, 400 nm, and 240 nm that can be well attributed to the band gaps of the nanocomposite components i.e. $Mn_2O_3$, ZnO, and MgO,

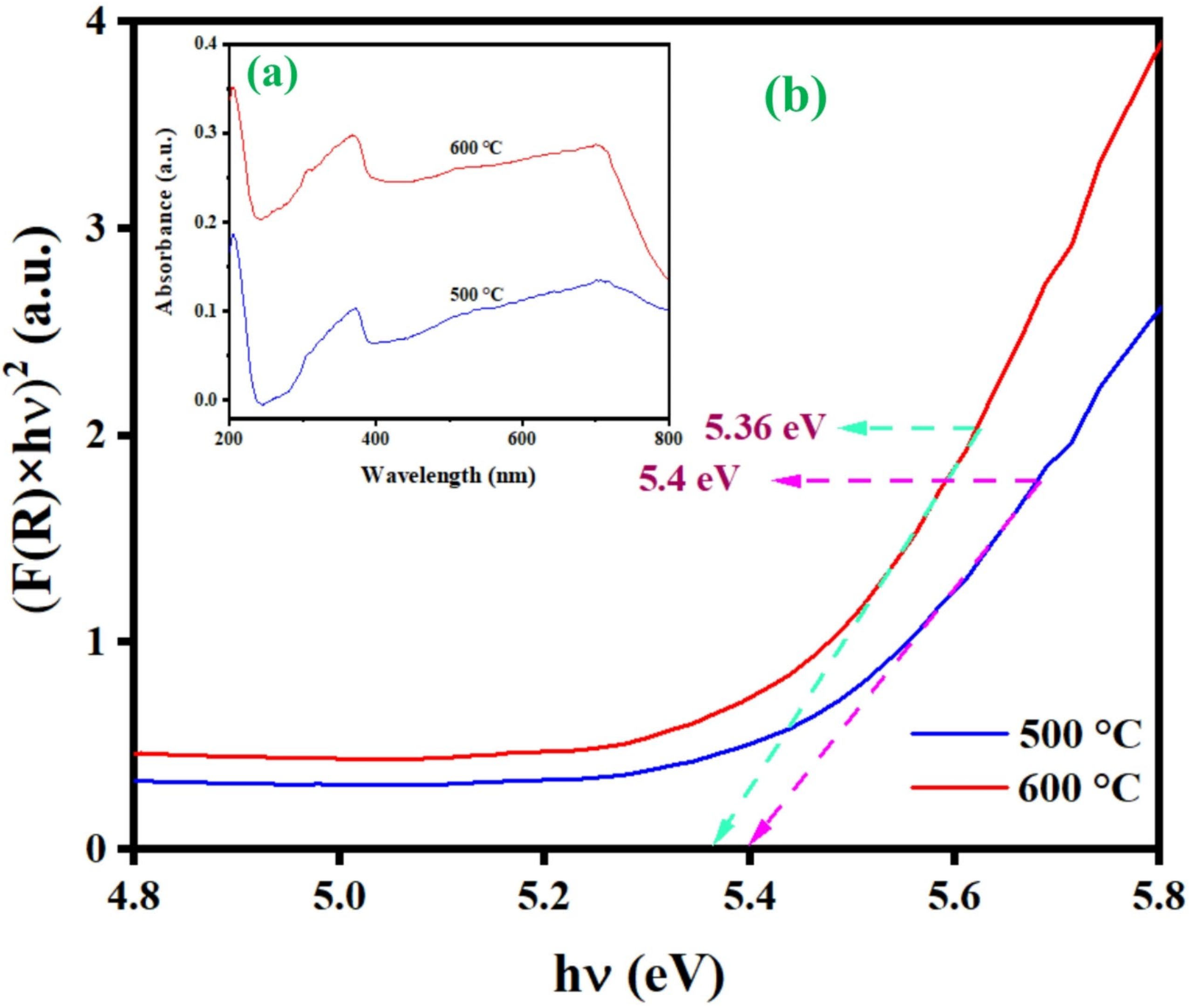

**Fig. 6**. Absorbance spectra (**a**) and Tauc plots (**b**) of ZnO-MgO-$Mn_2O_3$ nanocomposites.

respectively. However, the fundamental band gap of the synthesized nanocomposites as determined by Tauc method is close to the band gap of MgO component.

## Synthesis mechanism

In the synthesis process of ZnO-MgO-$Mn_2O_3$ nanocomposite, the phytochemicals in OBL extract act as reducing and masking agents that control the size, shape and stability of nanoparticles. Polyphenols, flavonoids and other bioactive compounds are extracted from basil seeds using water as a suitable solvent. Next, the reduction of metal ions occurs in such a way that the plant extract is added to metal ions ($Zn^{2+}$, $Mg^{2+}$, $Mn^{2+}$). The reducing agents in the extract, such as polyphenols, donate electrons to metal ions and reduce them to their elemental state. The following redox reactions (reactions 1–3) may occur here:

$$Zn^{2+} + 2e^{-} \rightarrow Zn^{0} \tag{1}$$

$$Mg^{2+} + 2e^{-} \rightarrow Mg^{0} \tag{2}$$

$$Mn^{2+} + 2e^{-} \rightarrow Mn^{0} \tag{3}$$

Atoms of the reduced metal combine to form a nucleus. On the other hand, capping agents from the extract adsorb onto the surface of the nuclei, preventing further growth and agglomeration. Nanoparticles grow through the addition of more metal ions and the subsequent reduction process. Next, metal nanoparticles are oxidized by oxygen in the air or by oxidizing agents in the solution. The oxidation process leads to the formation of metal oxide nanoparticles. The specific mechanism of oxidation may involve complex reactions including hydrolysis, condensation and redox reactions. Finally, individual metal oxide nanoparticles (ZnO, MgO, and $Mn_2O_3$) interact with each other through various mechanisms such as electrostatic interactions, hydrogen bonding, or covalent bonding to form the ZnO-MgO-$Mn_2O_3$ nanocomposite. These interactions leads to the formation of the nanocomposite with unique structure and properties.

In summary, according to the results, although the samples calcined at 500 °C and 600 °C are not significantly different in terms of crystalline structure, chemical composition, and optical properties. However, FE-SEM results showed that the particles calcined at 500 °C are more uniform with smaller particle size than the sample calcined at 600 °C. For this reason, this sample is selected for photocatalytic and cytotoxicity tests.

## Photocatalytic activity

When incident light of suitable energy interacts with the semiconductor photocatalyst material, valence band electrons absorb this energy and move to the conduction band with higher energy, leaving holes in the valence band[61]. In the valence band, water molecules generate hydroxyl radicals under oxidative reactions facilitated by holes[62]. Simultaneously, with the reduction of dissolved oxygen by electrons in the conduction band, superoxide anion radicals are produced[63]. Hydroxyl radicals and superoxide anions have strong redox properties that cause the oxidation of pollutants. Under certain conditions, superoxide anions may react with $h^+$ ions in the aqueous medium, leading to the generation of excess hydroxyl radicals ($OH^{\cdot}$). These radicals play an important role in further oxidation reactions. Hydroxyl radicals ($OH^{\cdot}$) produced during the process undergo rapid decomposition and contribute to redox reactions and continuous formation of hydroxyl radicals to drive the oxidation process forward. The detailed reactions of the photocatalytic mechanism are outlined in reactions 4–8, which elucidate the complex set of events leading to the degradation of pollutants and organic compounds.

$$h\nu \ + (ZnO - MgO - Mn_2O_3) \rightarrow \ h^+ + e^- \tag{4}$$

$$H_2O + h^+ \rightarrow \ H^+ + OH^{\cdot} \tag{5}$$

$$O_2 + \ e^- \rightarrow O^{\cdot}{}_2^{-} \tag{6}$$

$$\text{Dye} + \text{h}^+ \rightarrow \ \text{Oxidation products} \tag{7}$$

$$\text{Dye} + \text{e}^- \rightarrow \ \text{Reduction products} \tag{8}$$

Considering the importance of pH parameters, its effect on the removal of different dyes from aqueous solution was investigated. This research discusses how different pH levels affect the degradation/adsorption of dyes (MB, MO, EBT, and RhB) using ZnO-MgO-$Mn_2O_3$ nanocomposite. So, in conditions with a dye concentration of $10^{-5}$ M and catalyst concentration of $10^{-3}$ M, the effects of pH were investigated on the degradation process of MB (pH: 3, 7, and 10), RhB (pH: 3, 7, and 10), MO (pH: 3, 7, and 10), and EBT (pH: 3, 7, and 10) dyes. Based on the findings, with increasing pH, higher removal percentages were observed for MB (pH = 10, 99%), MO (pH = 10, 88.5%), and EBT (pH = 10, 97%) dyes, while for RhB dye, more removal percentage was detected at lower pH values (pH = 3, 86.9%) (Fig. 7). It was noticed that the surface uptake of MB and MO dyes was negligible as shown in Fig. 8a and c. However, Fig. 8b and d indicate that the surface adsorption of EBT dye under dark conditions was approximately 30, 40, and 50%, for the acidic, neutral, and alkaline conditions, respectively. For RhB, surface adsorption was observed only at pH = 3, with an approximate value of 20%, while negligible adsorption occurred at pH 7 and 10.

Also, the kinetic diagram of photocatalytic degradation of all dyes is presented in Fig. 8. The results show that all photocatalytic reactions follow pseudo-first-order kinetic. Based on the results, this nanocomposite had the best performance for MB dye at pH = 10 among other dyes. In the period between 0 and 15 min, a rapid increase in degradation was observed, followed by a slower rate. Also, the photocatalytic reaction constant obtained for MB, MO, RhB, and EBT are 0.068, 0.019, 0.025, and 0.020, respectively.

A comparison of the photocatalytic activity of the ZnO-MgO-$Mn_2O_3$ nanocomposite produced by the green chemistry method with ZnO and some other similar metal oxide nanocomposites is presented in Table 2 that demonstrated a promising photocatalytic performance of the synthesized sample in the degradation of dye pollutants. Also, a proposed mechanism of photocatalytic activity of the synthesized ZnO-MgO-$Mn_2O_3$ nanocomposite at 500 °C is represented graphically in Fig. 9 providing a visual guide to the sequence of steps involved in harnessing light energy for catalytic reactions and pollutant cleanup[64,65].

## Evaluation of anticancer activity

In this study, the cancerous 4T1 cells were grown in complete DMEM culture media under specific conditions and incubated (37 °C and 5% $CO_2$) for 24 h. To determine the selective toxicity of the synthesized ZnO-MgO-$Mn_2O_3$ nanocomposite, the cells were placed in a 96-well plate with a density of $1 \times 10^4$ cells per well. Next 24 h, the cells were treated with various concentrations of ZnO-MgO-$Mn_2O_3$ nanocomposite (7.5 to 1000 µg/mL). After 48 h, the culture medium was exchanged with fresh medium including MTT dye (5 mg/mL), and incubated for a further 4 h. The resulting insoluble formazan was dissolved in DMSO for 15 min. The absorbance of the dissolved formazan at 570 and 630 nm was measured to determine the number of viable cells using a specific Eq. (11). This experimental setup allowed for the evaluation of the synthesized ZnO-MgO-$Mn_2O_3$ nanocomposite impact on cancerous cell lines, providing insights into its potential as an anti-cancer agent[73].

$$\text{Cell survival } (\% \ ) = \text{Sample absorbance/ Control absorbance} \tag{11}$$

The results presented in Fig. 10 show that the green-synthesized ZnO-MgO-$Mn_2O_3$ nanocomposite has a significant cytotoxic impact on cancerous 4T1 cells (*P*-value less than 0.001). The calculated $IC_{50}$ value confirms the selectivity of ZnO-MgO-$Mn_2O_3$ nanocomposite in reducing the 4T1 cells' survival and the minimum $IC_{50}$

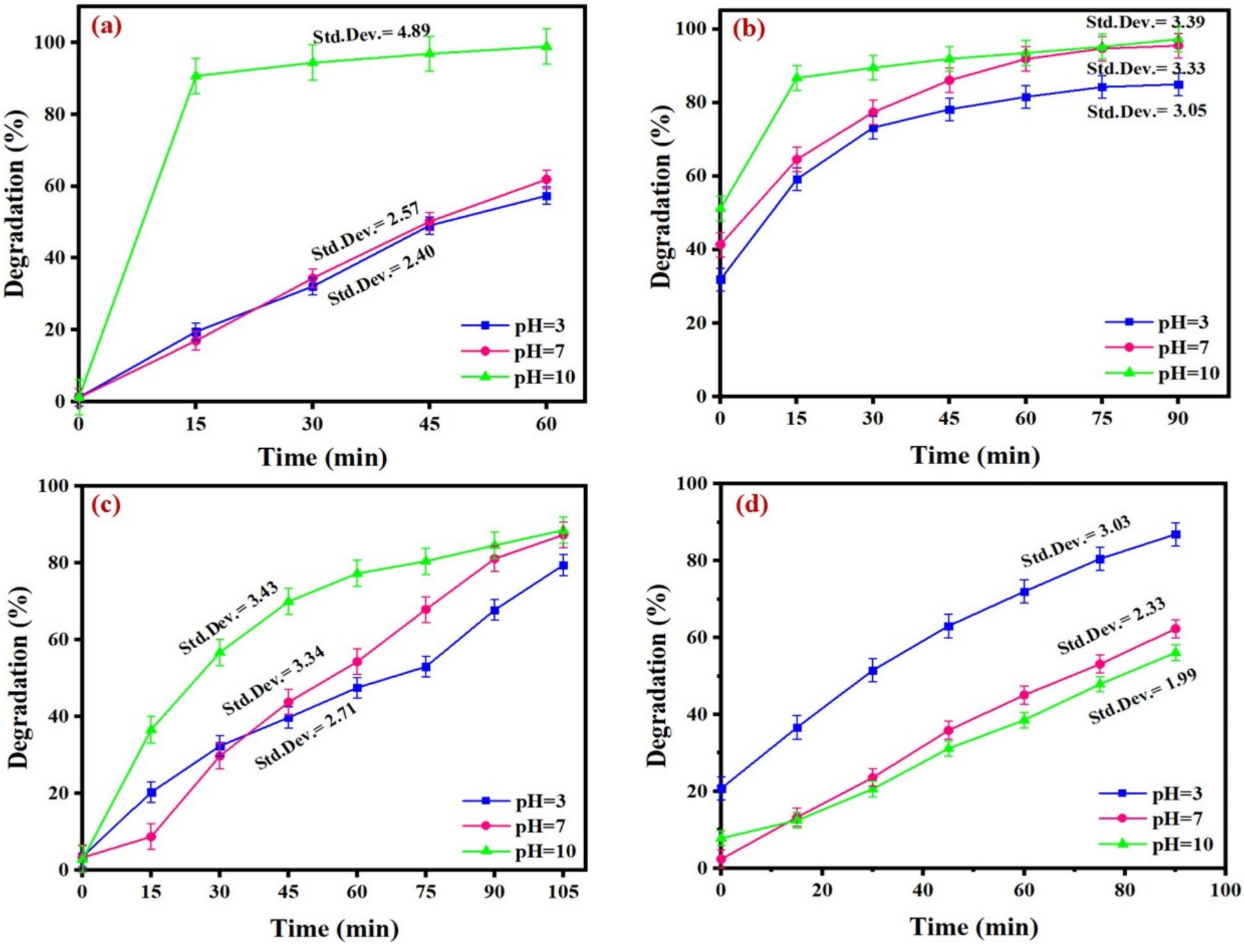

**Fig. 7**. The influence of pH on the degradation process of MB (**a**), EBT (**b**), MO (**c**), and RhB (**d**).

value was 323 µg/mL, indicating that 4T1 cells are sensitive to ZnO-MgO-$Mn_2O_3$ nanocomposite exposure at lower doses. Table 3 reportes anticancer activities of some different metal oxide nanocomposites to compare with the results of the present study.

## Conclusions

In this paper, novel ternary ZnO-MgO-$Mn_2O_3$ nanocomposites were successfully synthesized employing an environmentally friendly approach, using OBL seed extract under different temperature conditions (500 and 600 °C). By using a comprehensive set of analytical techniques including XRD, UV-Vis/DRS, FTIR, EDX, and FE-SEM, the structural features, dimensions, and morphology of the nanocomposite were investigated. XRD results verified formation of three different phases ofZnO, MgO, and $Mn_2O_3$ and it was observed that with the increase in the synthesis temperature, the crystallite size increased but the crystalline structure of the nanocomposites were almost similar. The DRS results showed not noticeable change of band gap values with calcination temperature, however, the samples exhibit high absorption in the wide range of the UV-Vis-NIR spectrum. Distinct absorption adges originated from consitutent metal oxides were detected in the absorption spectra of the synthesized ternary ZnO-MgO-$Mn_2O_3$ nanocomposite. On the other hand, by examining the photocatalytic activity, the effect of pH on the removal of four different dye pollutants from aqoues solution was tested. Based on the findings, with increasing pH, higher degradation percentages were observed for MB (pH = 10, 99%), MO (pH = 10, 88.5%), and EBT (pH = 10, 97%) dyes, while for RhB dye, more degradation percentage occurred at acidic pH (pH = 3, 86.9%). Finally, cytotoxicity evaluation of ZnO-MgO-$Mn_2O_3$ nanocomposite on 4T1 cancer cell line presented an $IC_{50}$ value of 323 µg/mL. These promising results are well applied to the use of ZnO-MgO-$Mn_2O_3$ nanocomposite in various applications, from industrial and biomedical sectors to a revolution in water and wastewater treatment and cancer treatment.

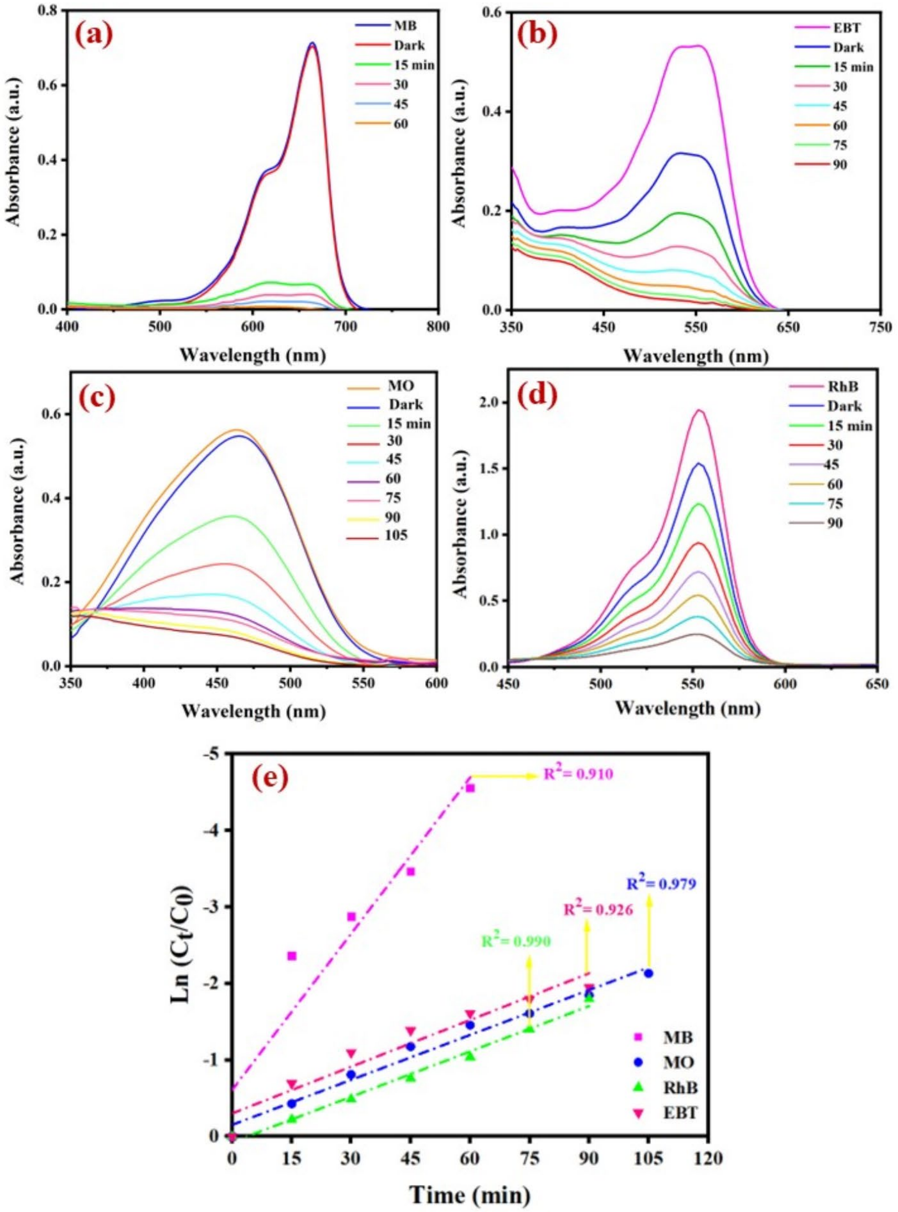

**Fig. 8**. Photocatalytic activities for MB (pH = 10, **a**), EBT (pH = 10, **b**), MO (pH = 10, **c**), and RhB (pH = 3, **d**), Pseudo-first-order kinetics (e).

| Photocatalyst | Dye | Time (min) | Degradation (%) | References |
|---|---|---|---|---|
| ZnO | Methylene blue | 90 | 92.6 | 66 |
| | Methyl orange | 90 | 90.5 | |
| | Rhodamine B | 75 | 93.2 | |
| | Pararosaniline | 75 | 92.9 | |
| ZnO-CdS-CdO | Methylene blue | 120 | 95 | 67 |
| | Rhodamine B | 120 | 95 | |
| N-doped ZnO/GO | Brilliant green | 90 | 100 | 68 |
| CuO/CuS/ZnO | Rhodamine B | 160 | 93.2 | 69 |
| ZnO/Au/Pd | Methylene blue | 180 | 97 | 70 |
| La-ZnO-GO | Eosin yellow | 210 | 100 | 71 |
| ZnO/g-$C_3N_4$/Ag | Methylene blue | 90 | 96 | 72 |
| | Malachite green | 90 | 99 | |
| ZnO-MgO-$Mn_2O_3$ | Methylene blue | 60 | 99 | Present work |
| | Methyl orange | 105 | 87.3 | |
| | Rhodamine B | 75 | 96.5 | |
| | Eriochrome Black T | 90 | 97.2 | |

**Table 2**. Comparison of the photocatalytic activity of the ZnO-MgO-$Mn_2O_3$ nanocomposite produced by the green chemistry method with some other similar nanocomposites described in the literatures.

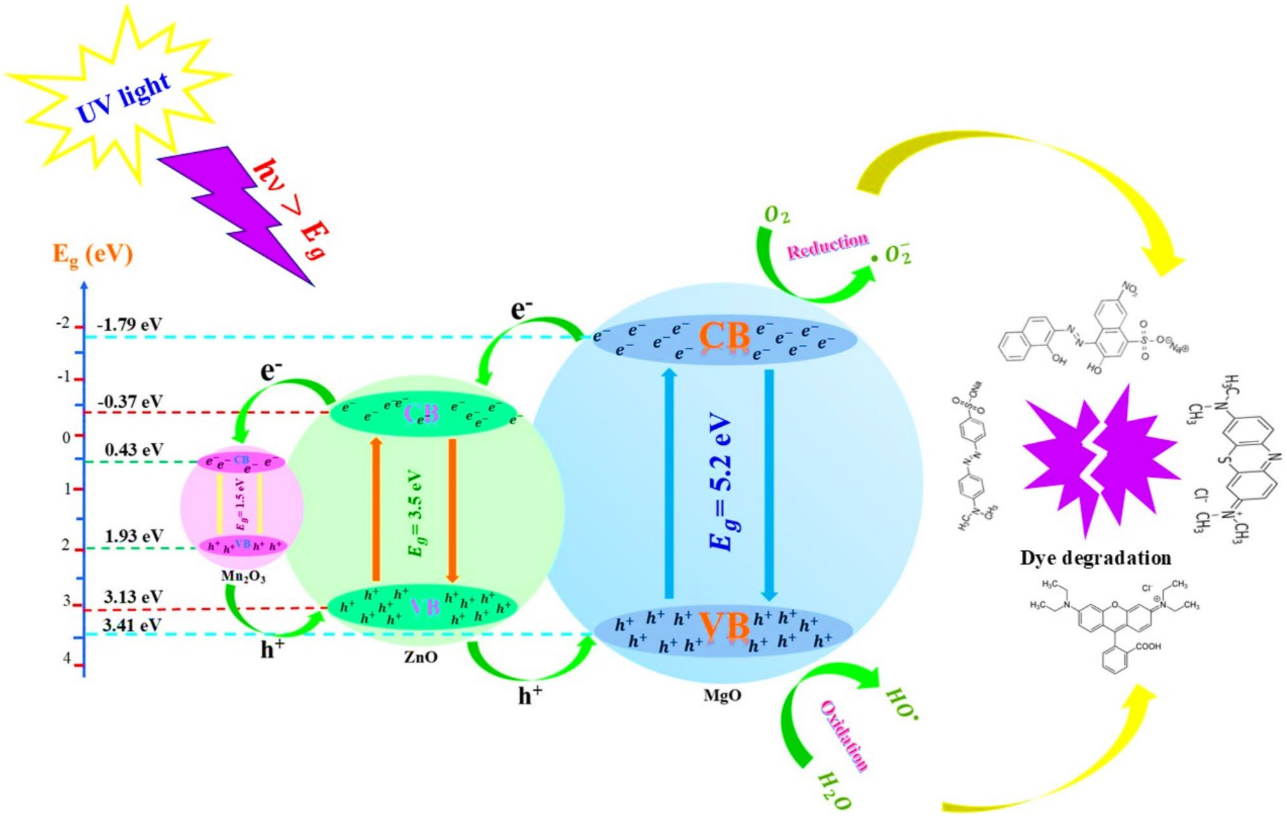

**Fig. 9**. The proposed mechanism of the photocatalytic process of ZnO-MgO-$Mn_2O_3$ nanocomposite.

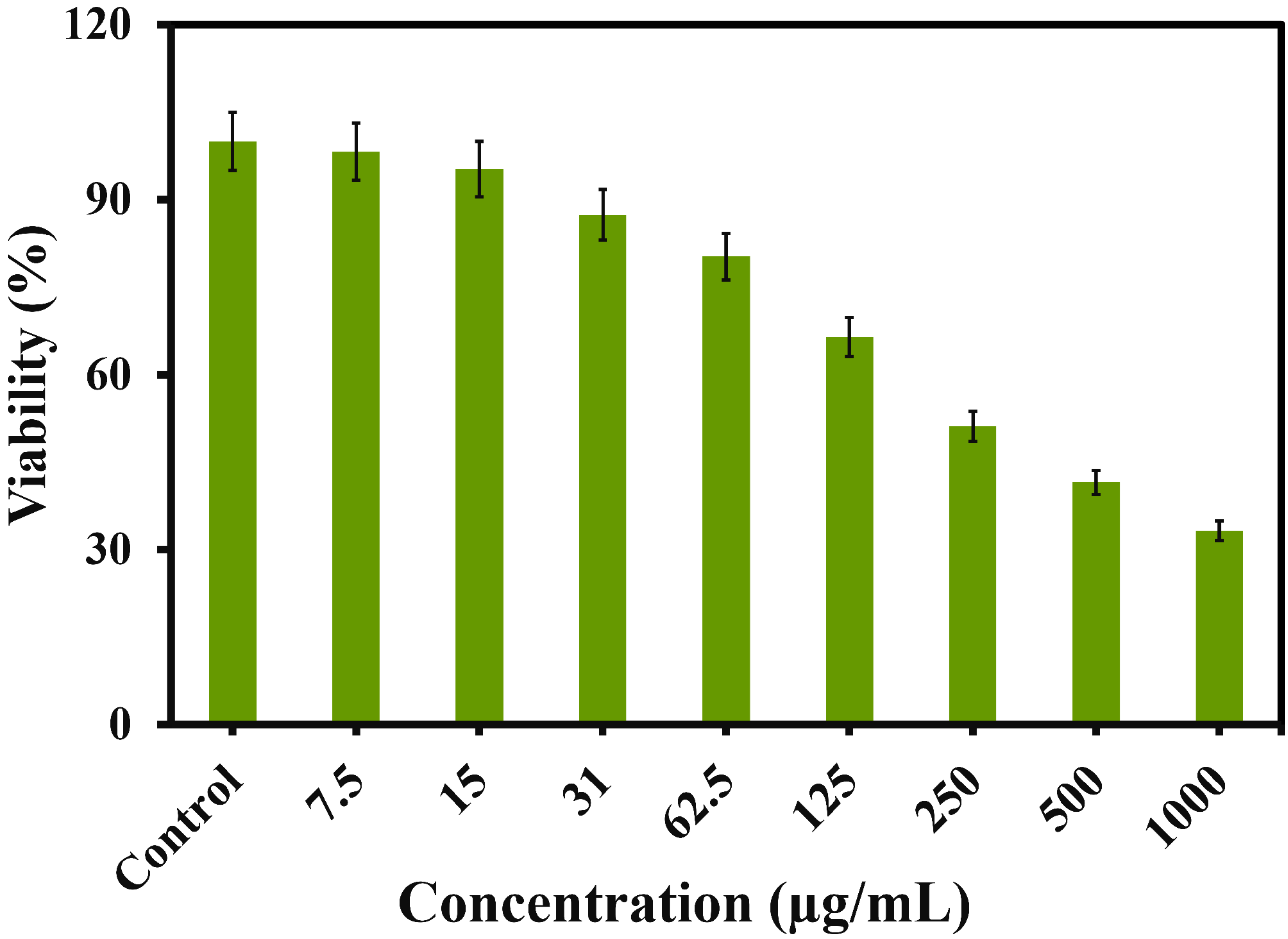

**Fig. 10**. Cytotoxicity test of the synthesized ZnO-MgO-$Mn_2O_3$ nanocomposite.

| Nanocomposite | Cell line | $IC_{50}$ (μg/mL) | References |
|---|---|---|---|
| Ag/Se doped ZnO–$Co_3O_4$-NiO | NIH3T3 | 258.5 | [74] |
| Ag/PVP @ $Y_2O_3$ | MCF-7 | 32.56 | [75] |
| ZnO/$TiO_2$/Ag | A549 | 120 | [76] |
| chitosan/$Fe_2O_3$/ZnO | WI-38 | 564.32 | [77] |
| $CeO_2$/CS/GO | MCF-7 | 125 | [78] |
| *Artemisia annua* L./ $Fe_3O_4$/$CeO_2$ (AFC) | 4T1 | 490.21 | [79] |
| ZnO-MgO-$Mn_2O_3$ | 4T1 | 323 | This work |

**Table 3**. Comparison of the anticancer activity of the ZnO-MgO-$Mn_2O_3$ nanocomposite produced by the green chemistry method with some other similar nanocomposites described in the literatures.

## Data availability

Data are available on request from corresponding authors (Fatemeh Shariatmadar Tehrani and Majid Darroudi).

Received: 23 August 2024; Accepted: 28 November 2024

## References

1. Araújo, E. S. et al. A review on the use of metal oxide-based nanocomposites for the remediation of organics-contaminated water via photocatalysis: fundamentals, bibliometric study and recent advances, *Toxics* **11** (8), 658 (2023).
2. Khatoon, U. T., Velidandi, A. & Rao, G. N. Sodium borohydride mediated synthesis of nano-sized silver particles: their characterization, anti-microbial and cytotoxicity studies. *Mater. Chem. Phys.* **294**, 126997 (2023).
3. Yoon, Y., Truong, P. L., Lee, D. & Ko, S. H. Metal-oxide nanomaterials synthesis and applications in flexible and wearable sensors. *ACS Nanosci. Au.* **2** (2), 64–92 (2021).

4. Khatoon, U. T., Velidandi, A. & Rao, G. N. Copper oxide nanoparticles: synthesis via chemical reduction, characterization, antibacterial activity, and possible mechanism involved. *Inorg. Chem. Commun.* **149**, 110372 (2023).
5. Yadav, S., Chauhan, M., Mathur, D., Jain, A. & Malhotra, P. Sugarcane bagasse-facilitated benign synthesis of $Cu_2O$ nanoparticles and its role in photocatalytic degradation of toxic dyes: a trash to treasure approach. *Environ. Dev. Sustain.* **23**, 2071–2091 (2021).
6. Nyabadza, A. et al. A review of physical, chemical and biological synthesis methods of bimetallic nanoparticles and applications in sensing, water treatment, biomedicine, catalysis and hydrogen storage. *Adv. Colloid Interface Sci.*, 103010 (2023).
7. Asghar, N. et al. Advancement in nanomaterials for environmental pollutants remediation: a systematic review on bibliometrics analysis, material types, synthesis pathways, and related mechanisms. *J. Nanobiotechnol.* **22** (1), 26 (2024).
8. Yadav, S., Sharma, T., Kaushik, R. & Malhotra, P. Peroxidase mimicking activity of *Saccharum officinarum* L. Capped gold nanoparticles using o-dianisidine as a substrate. *New J. Chem.* **47** (5), 2372–2382 (2023).
9. Yadav, S., Shah, A. & Malhotra, P. Orange pomace facilitated synthesis of $Cu_2O$/ZnO Nanocomposites for visual and optical sensing of silver ions in water for environmental remediation, *ChemistrySelect* **8** (2), e202203775 (2023).
10. Yadav, S., Chauhan, M., Jacob, M. & Malhotra, P. Distinguished performance of biogenically synthesized reduced-graphene-oxide-based mesoporous Au–Cu 2 O/RGO ternary nanocomposites for sonocatalytic reduction of nitrophenols in water. *New J. Chem.* **46** (20), 9685–9694 (2022).
11. Malhotra, S. P. K. & Alghuthaymi, M. A. Biomolecule-assisted biogenic synthesis of metallic nanoparticles, *Agri-Waste and Microbes for Production of Sustainable Nanomaterials*, 139–163 (2022).
12. Vankdoth, S., Velidandi, A., Sarvepalli, M. & Vangalapati, M. Poly-extract synthesized silver nanoparticles catalysed rhodamine-B and methyl orange dye degradation: influence of physicochemical parameters and their recyclability. *J. Nanoworld.* **8** (2), 42–54 (2022).
13. Yadav, S., Jain, A. & Malhotra, P. Bioinspired synthesis and green ecological applications of reduced graphene oxide based ternary nanocomposites. *Sustainable Mater. Technol.* **29**, e00315 (2021).
14. Khan, T., Jalal, H., Karam, K. & Khan, M. A. Biodegradable gum: a green source for silver nanoparticles, in Green Synthesis of Silver Nanomaterials: Elsevier, 189–217 (2022).
15. Gautam, Y. K., Sharma, K., Tyagi, S., Kumar, A. & Singh, B. P. Applications of green nanomaterials in coatings, in Green Nanomaterials for Industrial Applications: Elsevier, 107–152 (2022).
16. Vankdoth, S., Velidandi, A., Sarvepalli, M. & Vangalapati, M. Role of plant (tulasi, neem and turmeric) extracts in defining the morphological, toxicity and catalytic properties of silver nanoparticles. *Inorg. Chem. Commun.* **140**, 109476 (2022).
17. Sarvepalli, M., Velidandi, A. & Korrapati, N. Chemical vs biological silver nanoparticles: synthesis, characterization, properties, and in vitro applications. *Inorg. Chem. Commun.*, 112667 (2024).
18. Abdelsattar, A. S. et al. Green synthesis of silver nanoparticles using *Ocimum basilicum* L. and *Hibiscus sabdariffa* L. extracts and their antibacterial activity in combination with phage ZCSE6 and sensing properties. *J. Inorg. Organomet. Polym Mater.* **32** (6), 1951–1965 (2022).
19. Yadav, S., Shah, A. & Malhotra, P. Orange peel-derived $Cu_2O$/RGO nanocomposite: mesoporous binary system for degradation of doxycycline in water. *Environ. Dev. Sustain.* **26** (2), 4505–4532 (2024).
20. Naser, S. S. et al. Emerging trends in the application of green synthesized biocompatible ZnO nanoparticles for translational paradigm in cancer therapy. *J. Nanotheranostics*. **4** (3), 248–279 (2023).
21. Ghasemipour, P., Fattahi, M., Rasekh, B. & Yazdian, F. Developing the ternary ZnO doped $MoS_2$ nanostructures grafted on CNT and reduced graphene oxide (RGO) for photocatalytic degradation of aniline. *Sci. Rep.* **10** (1), 4414 (2020).
22. Gatou, M. A. et al. Magnesium Oxide (MgO) Nanoparticles: Synthetic strategies and biomedical applications, *Crystals* **14** (3), 215 (2024).
23. Nejati, M. et al. Green methods for the preparation of MgO nanomaterials and their drug delivery, anti-cancer and anti-bacterial potentials: a review. *Inorg. Chem. Commun.* **136**, 109107 (2022).
24. Taghavi Fardood, S. et al. Green synthesis and characterization of α-$Mn_2O_3$ nanoparticles for antibacterial activity and efficient visible-light photocatalysis. *Sci. Rep.* **14** (1), 6755 (2024).
25. Son, Y. H. et al. A rapid synthesis of mesoporous $Mn_2O_3$ nanoparticles for supercapacitor applications, *Coatings* **9** (10), 631 (2019).
26. Johnston, L. J., Du, X., Zborowski, A. & Kennedy, D. C. Characterization and cellular toxicity studies of commercial manganese oxide nanoparticles, *Nanomaterials* **14** (2), 198 (2024).
27. Zgura, I. et al. Cytotoxicity, antioxidant, antibacterial, and photocatalytic activities of ZnO–CdS powders, *Materials* **13** (01), 182 (2020).
28. Shubha, J. et al. ZnO/$La_2O_3$/NiO based ternary heterostructure nano-photocatalyst: preparation, characterization and its application for the degradation of methylene blue. *J. King Saud University-Science*. **34** (1), 101738 (2022).
29. Chauhan, M., Yadav, S. & Malhotra, P. In-situ biogenically synthesized $Cu_2O$/RGO composite using beetroot peel extract for selective and efficient reduction of cinnamaldehyde in water. *Appl. Nanosci.* **13** (6), 4331–4342 (2023).
30. Abdelbar, N. M., Ahmed, M. A. & Mohamed, A. A. A novel layered double hydroxide-based ternary nanocomposite for the effective photocatalytic degradation of rhodamine B. *RSC Adv.* **14** (21), 14523–14538 (2024).
31. Sabouri, Z. et al. Phytoextract-mediated synthesis of Ag-doped ZnO–MgO–CaO nanocomposite using *Ocimum Basilicum* L. seeds extract as a highly efficient photocatalyst and evaluation of their biological effects. *Ceram. Int.* **49** (12), 20989–20997 (2023).
32. Ali, M. H., Abdelkarim, M. S. & Al-Afify, A. D. Characterization and photodegradation of methylene blue dye using bio-synthesized cerium oxide nanoparticles with Spirulina platensis extract. *Discover Appl. Sci.* **6** (3), 1–17 (2024).
33. Albeladi, A. et al. $Fe_3O_4$-CdO Nanocomposite for organic dye photocatalytic degradation: synthesis and characterization, *Catalysts* **14** (1), 71 (2024).
34. Xie, W. et al. Degradation of Organic dyes by the UCNP/h-BN/$TiO_2$ Ternary photocatalyst. *ACS Omega*. **8** (51), 48662–48672 (2023).
35. Shabil Sha, M. et al. Photocatalytic degradation of organic dyes using reduced graphene oxide (rGO). *Sci. Rep.* **14** (1), 3608 (2024).
36. Tran, H. N. Applying linear forms of pseudo-second-order kinetic model for feasibly identifying errors in the initial periods of time-dependent adsorption datasets, *Water* **15** (6), 1231 (2023).
37. Ahmad, N. et al. Insight into the adsorption thermodynamics, kinetics, and photocatalytic studies of polyaniline/$SnS_2$ nanocomposite for dye removal. *J. Hazard. Mater. Adv.* **10**, 100321 (2023).
38. Greeshma, K., Muthulingam, S., Thamizselvi, R. & Sen, D. B. Antimicrobial studies and characterization of ZnO nanoparticles by chemical method. *GSC Adv. Res. Reviews*. **8** (2), 071–077 (2021).
39. Abdelghani, G. M., Ahmed, A. B. & Al-Zubaidi, A. B. Synthesis, characterization, and the influence of energy of irradiation on optical properties of ZnO nanostructures. *Sci. Rep.* **12** (1), 20016 (2022).
40. Hirphaye, B. Y., Bonka, N. B., Tura, A. M. & Fanta, G. M. Biosynthesis of magnesium oxide nanoparticles using Hagenia Abyssinica female flower aqueous extract for characterization and antibacterial activity. *Appl. Water Sci.* **13** (9), 175 (2023).
41. Todan, L. et al. Comparative study of MgO nanopowders prepared by different chemical methods. *Gels* **9** (8), 624 (2023).
42. Gomaa, I., Abdel-Salam, A. I., Khalid, A. & Soliman, T. Fabrication, structural, morphological, and optical features of $Mn_2O_3$ polyhedron nano-rods and $Mn_2O_3$/reduced graphene oxide hybrid nanocomposites. *Opt. Laser Technol.* **161**, 109126 (2023).
43. Al-Bagawi, A. H. Green synthesis of mesoporous 2D $Mn_2O_3$/rGO nanocomposite for effective removal of methyl orange. *Water Pract. Technol.* **18** (6), 1317–1330 (2023).

44. Kawsar, M., Hossain, M. S., Bahadur, N. M. & Ahmed, S. Synthesis of nano-crystallite hydroxyapatites in different media and a comparative study for estimation of crystallite size using Scherrer method, Halder-Wagner method size-strain plot, and Williamson-Hall model. *Heliyon* **10** (3) (2024).
45. Muthee, D. K. & Dejene, B. F. Effect of annealing temperature on structural, optical, and photocatalytic properties of titanium dioxide nanoparticles. *Heliyon* **7** (6) (2021).
46. Mobarak, M. B., Hossain, M. S., Chowdhury, F. & Ahmed, S. Synthesis and characterization of CuO nanoparticles utilizing waste fish scale and exploitation of XRD peak profile analysis for approximating the structural parameters. *Arab. J. Chem.* **15** (10), 104117 (2022).
47. Lam, N. H. et al. Evaluation of the structural deviation of Cu/$Cu_2O$ nanocomposite using the X-ray diffraction analysis methods. *Crystals* **12** (4), 566 (2022).
48. Disha, S. A., Hossain, M. S., Habib, M. L. & Ahmed, S. Calculation of crystallite sizes of pure and metals doped hydroxyapatite engaging Scherrer method, Halder-Wagner method, Williamson-Hall model, and size-strain plot. *Results Mater.* **21**, 100496 (2024).
49. Shaik, K. & Cole, S. Comparative study of crystallite size from XRD and TEM results for pure and $V_2O_5$ doped CdO-$FePO_4$ composite nanopowders. *Phys. Chem. Res.* **11** (2), 241–251 (2023).
50. Rabiei, M. et al. Comparing methods for calculating nano crystal size of natural hydroxyapatite using X-ray diffraction. *Nanomaterials* **10** (9), 1627 (2020).
51. Aghazadeh, M. & Aghazadeh, F. Green chemistry method with XRD analyzes and absorption of $TiO_2$ nanoparticles modified with use of choline chloride. *Int. J. Bio-Inorg Hybr Nanomater*. **7** (2), 97–108 (2018).
52. Rada, R. et al. Development of iron–silicate composites by waste glass and iron or steel powders. *Molecules* **28** (17), 6296 (2023).
53. Shaheen, I. et al. Facile synthesis of ZnO–$CoMoO_4$ nanocomposite using bio-organic fuel for energy storage application. *J. Mater. Sci.: Mater. Electron.* **32**, 8460–8474 (2021).
54. Dal Poggetto, G. et al. FT-IR study, thermal analysis, and evaluation of the antibacterial activity of a MK-geopolymer mortar using glass waste as fine aggregate. *Polymers* **13** (17), 2970 (2021).
55. Baral, S. C. et al. Enhanced photocatalytic degradation of organic pollutants in water using copper oxide (CuO) nanosheets for environmental application. *JCIS Open.* **13**, 100102 (2024).
56. Haryński, Ł., Olejnik, A., Grochowska, K. & Siuzdak, K. A facile method for Tauc exponent and corresponding electronic transitions determination in semiconductors directly from UV–Vis spectroscopy data. *Opt. Mater.* **127**, 112205 (2022).
57. Li, J., Xie, D., Li, M., Liu, S. & Wei, C. A. Optimal learning samples for two-constant Kubelka-Munk theory to match the color of pre-colored fiber blends. *Front. NeuroSci.* **16**, 945454 (2022).
58. Pacheco, M. A. L., Rojas, J. J. B., Castro-Ramos, J., Manríquez, J. F. V. & Esmonde-White, K. Optical study to identify and quantify capsaicin in optical window. *Heliyon* **7** (3) (2021).
59. Haiouani, K., Hegazy, S., Alsaeedi, H., Bechelany, M. & Barhoum, A. Green Synthesis of Hexagonal-like ZnO nanoparticles modified with phytochemicals of clove (Syzygium aromaticum) and thymus capitatus extracts: enhanced antibacterial, antifungal, and antioxidant activities. *Materials* **17** (17), 4340 (2024).
60. Mahadevaiah, R., Lalithamba, H. S., Shekarappa, S. & Hanumanaika, R. Synthesis of Nα-protected formamides from amino acids using MgO nano catalyst: study of molecular docking and antibacterial activity. *Scientia Iranica*. **24** (6), 3002–3013 (2017).
61. Tahir, M. B., Sohaib, M., Sagir, M. & Rafique, M. Role of nanotechnology in photocatalysis. *Encyclopedia Smart Mater.* 578, (2022).
62. Pavel, M. et al. Photocatalytic degradation of organic and inorganic pollutants to harmless end products: assessment of practical application potential for water and air cleaning. *Catalysts* **13** (2), 380 (2023).
63. Wang, G. R. & Huang, M. H. Photocatalytic oxidative cyclization of aromatic thioamides catalyzed by $Cu_2O$ rhombic dodecahedra. *J. Mater. Chem. A* (2024).
64. Xu, X. et al. Mechanisms for· $O_2$-and ·OH production on flowerlike $BiVO_4$ photocatalysis based on electron spin resonance. *Front. Chem.* **6**, 64 (2018).
65. Sakar, M., Mithun, R., Prakash & Do, T. O. Insights into the $TiO_2$-based photocatalytic systems and their mechanisms, *Catalysts*, vol. 9, no. 8, p. 680, (2019).
66. Gowthambabu, V., Balamurugan, A., Satheeshkumar, S. & Kanmani, S. ZnO nanoparticles as efficient sunlight driven photocatalyst prepared by solution combustion method involved lime juice as biofuel. *Spectrochim. Acta Part A Mol. Biomol. Spectrosc.* **258**, 119857 (2021).
67. Das, D. & Nandi, P. Ternary ZnCdSO composite photocatalyst for efficient dye degradation under visible light retaining Z-scheme of migration pathways for the photogenerated charge carriers. *Sol. Energy Mater. Sol. Cells.* **217**, 110674 (2020).
68. Peter, C. et al. N-doped ZnO/graphene oxide: a photostable photocatalyst for improved mineralization and photodegradation of organic dye under visible light. *Ionics* **25**, 327–339 (2019).
69. Cao, F., Pan, Z. & Ji, X. Enhanced photocatalytic activity of a pine-branch-like ternary CuO/CuS/ZnO heterostructure under visible light irradiation. *New J. Chem.* **43** (28), 11342–11347 (2019).
70. Lee, S. J. et al. ZnO supported Au/Pd bimetallic nanocomposites for Plasmon improved photocatalytic activity for methylene blue degradation under visible light irradiation. *Appl. Surf. Sci.* **496**, 143665 (2019).
71. Oppong, S. O. B., Anku, W. W., Opoku, F., Shukla, S. K. & Govender, P. P. Photodegradation of eosin yellow dye in water under simulated solar light irradiation using La–doped ZnO nanostructure decorated on graphene oxide as an advanced photocatalyst. *ChemistrySelect* **3** (4), 1180–1188 (2018).
72. Ravichandran, K. & Sindhuja, E. Fabrication of cost effective g-$C_3N_4$ + ag activated ZnO photocatalyst in thin film form for enhanced visible light responsive dye degradation. *Mater. Chem. Phys.* **221**, 203–215 (2019).
73. Kermani, M., Mostafapour, A., Sabouri, Z., Gheibihayat, S. M. & Darroudi, M. The photocatalytic, cytotoxicity, and antibacterial properties of zinc oxide nanoparticles synthesized using *Trigonella foenum-graecum* L. extract. *Environ. Sci. Pollut. Res.* **30** (7), 19313–19325 (2023).
74. Sabouri, Z., Sammak, S., Sabouri, S., Moghaddas, S. & Darroudi, M. Green synthesis of Ag-Se doped ZnO-Co3O4-NiO fivenary nanocomposite using poly anionic cellulose and evaluation of their anticancer and photocatalyst applications. *Chem. Methodol.* **8** (3), 164–176 (2024).
75. Krishna, S. & Myvizhi, G. and *A Biocompatible Polyvinyl Pyrrolidone/Silver-capped Ytrrium Oxide Ternary Nanocomposites for Pharmaceutical Applications* (Antioxidant and Cytotoxicity activities, 2024).
76. Sakthi Mohan, P. et al. Facile in-situ fabrication of a ternary ZnO/$TiO_2$/Ag nanocomposite for enhanced bactericidal and biocompatibility properties. *Antibiotics* **10** (1), 86 (2021).
77. Al-Rajhi, A. M. et al. The green approach of chitosan/$Fe_2O_3$/ZnO-nanocomposite synthesis with an evaluation of its biological activities. *Appl. Biol. Chem.* **67** (1), 75 (2024).
78. Saranya, J. et al. Development of cerium oxide/chitosan/graphene oxide nanocomposite: An investigation toward its biological applications under in vitro conditions, *Crystals*, vol. 13, no. 9, p. 1393, (2023).
79. Ahmadi, Z., Bayrami, A., Zahri, S., Rahim Pouran, S. & Habibi-Yangjeh, A. Antineoplastic activity of Artemisia annua bio-united $Fe_3O_4$/$CeO_2$ on 4T1 breast cancer cells: in vivo and in vitro. *Cancer Nanotechnol.* **15** (1), 53 (2024).

## Acknowledgements

The technical support for this work was provided by the University of Semnan and Mashhad University of Medical Sciences based on the Ph.D. thesis of Ms. R. Hazrati Saadabadi.

## Author contributions

R. H. S.: Data acquisition, Investigation, Analysis, and Writing an original draft. F. S.T: Supervision, Project administration, Funding, and Resources acquisition, Review & Editing. Z.S.: Data acquisition, Investigation, Analysis, and Writing - Review & Editing. M. D.: Supervision, Project administration, Funding, and Resources acquisition, Review & Editing.

## Declarations

## Competing interests

The authors have declared no conflict of interest.

## Ethical approval

For this type of study, ethical approval was not.

## Additional information

**Correspondence** and requests for materials should be addressed to F.S.T. or M.D.

**Reprints and permissions information** is available at www.nature.com/reprints.